High Efficiency 2-Bladed Utility Wind Turbine Enhanced by CoFlow Jet Active Flow Control

Yan Ren [*], Gecheng Zha [†]
CoFlow Jet Wind Turbines, LLC
PO Box 244681, Coral Gables, Florida 33124

Nick Johnson [‡]
Ganesh Vijayakuma [§]
National Renewable Energy Laboratory, Golden, CO 80401

Abstract

The aerodynamic performance and power output of a high efficiency Co-Flow Jet (CFJ) 2-bladed Wind Turbine is studied in this paper. CFJ is a Zero-Net-Mass-Flux (ZNMF) active flow control method that dramatically increases airfoil lift coefficient and suppresses flow separation at a low energy expenditure. The 3D Reynolds Averaged Navier-Stokes (RANS) equations with one-equation Spalart-Allmaras (SA) turbulence model are solved to simulate the 3D flows of the wind turbines. The CFJ-Wind Turbine in this paper is modified from the NREL 3-bladed 3.4 MW reference wind turbine with the same RPM, blade length, distribution of chord, twist, and bending. The CFJ 2-bladed wind turbine utilizes the CFJ-NACA 64 series airfoils at most of the blade span from 31.88% to the tip. The CFJ injection and suction slots are implemented along the full blade span to enhance the effectiveness and power output. The study shows that the 2-bladed CFJ turbine significantly increases power output compared with the 3-bladed baseline turbine at all wind speeds by 15.8% at the wind speed of 9.8 m/s and by 25.9% at 4 m/s respectively. The efficiency enhancement is substantially more at the low wind speed than at high wind speed. This would be very beneficial to increase the annual power output or capacity factor as wind turbines work at the speeds lower than the rated speed for most of the time. The results show that the flow field around the blade surface presents a significant enhanced suction peak near the blade leading edge, which results in a very high tangential force and thus increased wind turbine net power coefficient. Consistent with the previous study for the small NREL Phase VI research wind turbine, this paper demonstrates that CFJ 2-bladed wind turbine is an effective technology to extract more power from the wind at all speeds. This study is just an initial effort to demonstrate the advantage of the CFJ blade with no design optimization. It is believed that there is more potential to further enhance the efficiency improvement.

Nomenclature

CFJ	Co-flow jet
U	Flow Velocity
ρ	Air Density
AoA	Angle of Attack

[*] Ph.D., Chief Engineer, yren@coflowjetwindturbines.com
[†] Ph.D., Chairman, Professor of the University of Miami, gzha@coflowjetwindturbines.com
[‡] NREL Researcher IV
[§] NREL Researcher - Mechanical Engineering

$\dot{m}$	Mass Flow Rate
M	Mach Number
Re	Reynolds Number
L	Aerodynamics Lift
D	Aerodynamic Drag
n	Turbine blade number
R	Turbine rotor disk radius
θ	Turbine blade pitch angle
F_t	Turbine blade tangential force
F_a	Turbine blade axle force
T_s	Turbine spinning torque, $T_s = \int_0^R r \cdot dF_t$
T_b	Turbine bending torque, $T_b = \int_0^R r \cdot dF_a$
τ_s	Turbine radial spinning torque coefficient
p	Static Pressure
p_0	Total Pressure
η	Pumping Power
q_∞	Freestream Dynamic Head, $\frac{1}{2}\rho_\infty u_\infty{}^2$
C_M	Moment Coefficient, $\frac{M}{q_\infty S c}$
C_p	Pressure Coefficient, $\frac{p-p_\infty}{q_\infty}$
C_μ	Jet Momentum Coefficient, $\frac{\dot{m_j} v_j}{q_\infty S}$
C_{pr}	Wind turbine blade power coefficient
C_{pw}	Wind turbine Net power coefficient
P_{net}	Wind turbine Net power
∞	Free Stream Conditions

1 Introduction

Wind energy is the fastest growing energy sector due to its sustainability, renewability and zero direct emission. Therefore, wind turbines, the machinery to extract wind energy, have been widely studied. The most important aerodynamic measure of merit of wind turbines is their power output, in particular at the speed lower than the rated speed that the turbines will work for most of the time in a year. When the wind speed is too high, the power output of a wind turbine needs to be limited to avoid the failure of the wind turbine structure and the electric generator system. Typically, a turbine is designed to have an optimum efficiency at a certain ratio of the tip speed to the freestream flow speed. When the freestream velocity is greater or smaller than that, the efficiency may drop and may be compensated by varying the pitch angle or the rotational speed.

The other important issue for wind turbine aerodynamic design is to increase wake and unsteady flow (e.g. gusts) resistance without stalling the blades. Wakes in wind farms and unsteady gusts can severely penalize the wind turbine efficiency and reduce turbine life span due to dynamic loads. To increase wind turbine power output and mitigate flow fluctuation, passive and active flow control methods have been implemented on wind turbine blades.

An aerodynamic technology that can increase the lift coefficient and the ratio of lift to drag without stalling the blade is appealing. This is the motivation of the present study to utilize active flow control with distributed aerodynamic devices on the blade, which is identified as one of the most promising directions for wind turbine

development[1].

The recently developed Co-flow Jet (CFJ) flow control is a zero-net-mass-flux (ZNMF) active flow control that is able to dramatically enhance the airfoil performance at low energy expenditure[2, 3, 4, 5, 6, 7, 8, 9, 10]. As shown in Fig. 1, a CFJ airfoil withdraws a small amount of mass flow from trailing edge, pressurizes it by a series of low pressure fans, and injects the flow at leading edge tangential to the mainstream. It is demonstrated numerically and experimentally that CFJ achieves radical lift augmentation, drag reduction and stall angle of attack increase [2, 3, 4, 5, 6, 7, 8]. Lefebvre and Zha[11] implement CFJ on a pitching airfoil and basically remove its hysteresis. The system energy analysis indicates that the CFJ energy consumption is absorbed by the controlled flow to increase the system capability doing work[9], which provides the CFJ flow control with a low energy expenditure in adverse pressure gradient[10].

Xu and Zha [12] apply CFJ to S809 wind turbine airfoil and achieved an optimal configuration of CFJ-S809 airfoil with significant improvement of C_L and aerodynamic efficiency $(C_L/C_D)_c$. Xu and Zha [13] further numerically applied CFJ-S809 airfoil to the NREL Phase VI 10 m diameter horizontal axis wind turbine [14] with a significant efficiency improvement. Ren and Zha [15] applied an optimized CFJ-NACA-6421 airfoil instead of using S809 airfoil and are able to increase the power coefficient even more by 35% at the same pitch angle of the baseline wind turbine. However, the NREL Phase VI wind turbine[14] is a small research turbine. The Reynolds number and the variation of the blade geometry and flow along the blade span is substantially less than a utility turbine with a very long blade length.

The purpose of this paper is to apply CFJ technology to a 2-bladed 3.4 MW utility wind turbine to demonstrate its high efficiency performance. The 3-bladed 3.4 MW Reference Wind Turbine (RWT) designed by a joint team led by National Renewable Energy Laboratory (NREL) [16] is used for comparison reference. The CFJ 2-bladed Wind Turbine is modified from the RWT by removing one blade and using CFJ NACA 64 series airfoil at most of the span. The corresponding RPM, blade length, chord, twisting, and bending distributions are kept the same.
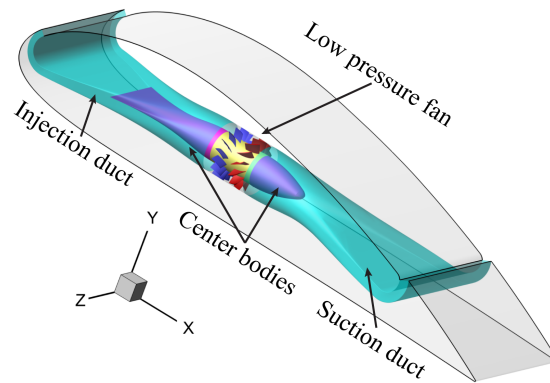

Figure 1: Schematics of the CFJ airfoil with embedded micro-compressor

2 Aerodynamic Forces and Power

The velocity determining the aerodynamic force acting on a wind turbine blade at a radius r is the relative velocity, also called apparent wind velocity as labeled in Fig. 2. The airfoil will generate a lift and drag as illustrated in Fig. 2. The tangential force rotates the blades and generates power output.

The tangential force at radius r can be expressed as:

$$dF_t = dL\cos(\alpha) - dD\sin(\alpha) = n(0.5\rho V_{rel}^2)C_L[\cos(\alpha) - \frac{1}{C_L/C_D}\sin(\alpha)]cdr \tag{1}$$

where L stands for the lift, D for the drag, V_{rel} is the relative velocity at radius r, α is the angle between the relative velocity and the turbine axis as shown in Fig. 2, C_L and C_D are the airfoil lift and drag coefficient, c is the airfoil chord at radius r, and n is the number of blades.

The total power output of a wind turbine is the torque multiplied by angular velocity. Based on Eq. (3), the power coefficient is calculated as:

$$C_{pr} = \frac{n}{\pi} \int_{\bar{R}_{root}}^{\bar{R}_{tip}} \bar{\rho}\bar{V}_{rel}^2 C_L[\cos(\alpha) - \frac{1}{C_L/C_D}\sin(\alpha)]\bar{c}\overline{\omega R}d\bar{R} \tag{2}$$

where ω is the angular velocity of the blades. All the variables with overhead bar stand for normalized variables as: $\bar{R} = r/R$, $\bar{\rho} = \rho/\rho_\infty$, $\bar{V}_{rel} = V_{rel}/V_\infty$, and $\overline{\omega R} = \omega r/V_\infty$.

The flow angle α, which is determined by the ratio of the incoming wind speed and blade rotating speed, is also important to determine the optimum power coefficient as shown in Eq. (2). The wind turbine research community in general adopts the ratio of the blade tip speed to wind speed in the range of 7 to 10[17], which then determines the α distribution along the blade. A turbine blade is usually twisted to have the optimum angle of attack along the span.
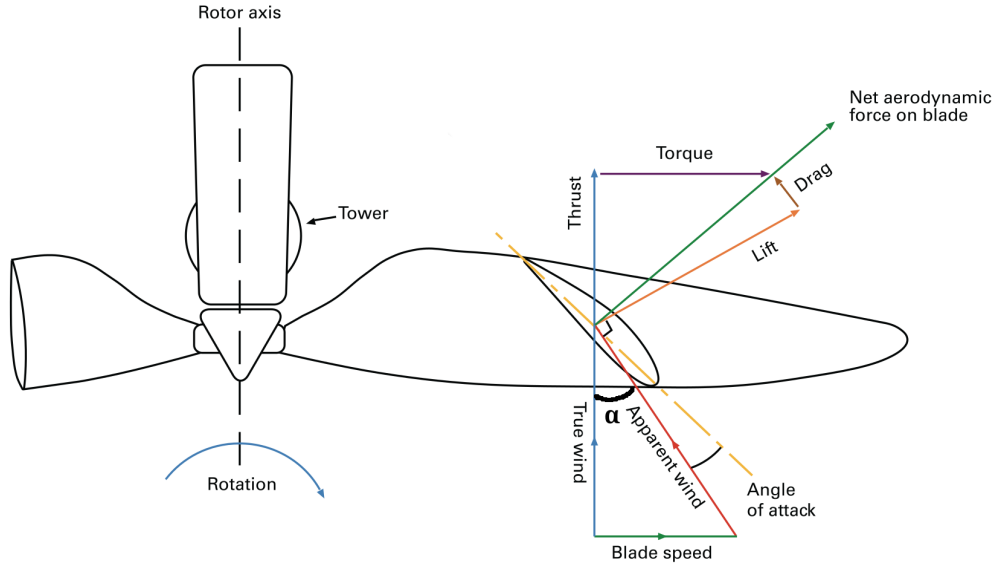

Figure 2: Aerodynamic forces acting on a wind turbine airfoil at a certain radius(plot modified from [18]).

Eq. (2) indicates that both a high lift coefficient and a high C_L/C_D are beneficial to increase the power coefficient. Usually, the angle of attack(AoA) for maximum C_L/C_D is fairly low such as about $3°$ to $5°$. The maximum C_L would occur near stall and the AoA is high and should be avoided. Typical wind turbines select the design AoA to favor maximum C_L/C_D to have enough stall margin. Thumthae and Chitsomboon suggest that the optimum AoA should be between the one for maximum C_L/C_D and maximum C_L[19]. Huyer et al indicate that wind turbines must be designed to achieve the maximum efficiency at or near the static stall AoA since the

AoA of dynamic stall usually occurs at an AoA higher than the static stall AoA [20]. The CFJ wind turbines are aimed at dramatically increasing C_L and C_L/C_D with high stall margin, and at the same time using minimal energy expenditure to achieve net power output gain.

The wind turbine radial performance is described by turbine radial spinning torque coefficient τ_s, which is defined as:

$$\tau_s = \frac{r \int_l p\,dl_t}{\frac{1}{2}\rho_\infty u_\infty^2 R^2} n \tag{3}$$

where r is the radius of a specific turbine radial location, p is the static pressure, l is the cross-sectional contour of the blade at the radial location, subscript t stands for the tangential direction, n is the number of blades of a turbine. τ_s describes the turbine spinning torque distribution along the radial direction.

3   The Co-Flow Jet Wind Turbine Parameters

To facilitate the description of CFJ wind turbine performance, several important parameters are given below.

3.1   Jet Momentum Coefficient

The injection jet momentum coefficient C_μ is used to describe the CFJ strength as:

$$C_\mu = \frac{\dot{m}V_j}{\frac{1}{2}\rho_\infty U_\infty^2 A_{ref}} \tag{4}$$

where $\dot{m}$ is the injection mass flow, V_j is the mass-averaged injection relative velocity, ρ_∞ denotes the free stream density, and A_{ref} is the reference area defined as the disk area of the wind turbine, U_∞ is the freestream velocity.

3.2   Co-Flow Jet Power Coefficient

The CFJ power required is determined by the total enthalpy rise in the turbine rotating frame from the suction duct outlet to the injection duct inlet [21, 13]. The total enthalpy rise can be achieved by the embedded fans. The power required by the CFJ can be expressed as:

$$P = \frac{\dot{m}H_{t2}}{\eta}(\Gamma^{\frac{\gamma-1}{\gamma}} - 1) \tag{5}$$

where, $\dot{m}$ is the CFJ mass flow rate, H_{t2} is the total enthalpy in the turbine rotating frame at the suction slot, Γ is the total pressure ratio in the turbine rotating frame between the injection and suction, and η is the pumping system efficiency. For the CFJ wind turbine, the $\dot{m}$, H_{t2} and Γ are calculated in the rotational frame of reference using relative properties.

Eq. (5) indicates that the power required by the CFJ is linearly determined by the mass flow rate and exponentially by the total pressure ratio. This relationship in fact applies to all the active flow controls based on fluidic actuators. The power coefficient is defined as:

$$P_c = \frac{P}{\frac{1}{2}\rho_\infty U_\infty^3 A_{ref}} \tag{6}$$

where P is the CFJ required power defined in Eq. (5).

3.3 CFJ Wind Turbine Net Power Coefficient

The wind turbine net power coefficient C_{pw} is commonly used to designate the efficiency of the entire turbine power system. For a conventional wind turbine, the C_{pw} is defined as:

$$C_{pw} = C_{pr} = \frac{P_w}{\frac{1}{2}\rho_\infty U_\infty^3 A_{ref}} \tag{7}$$

where P_w is the wind turbine rotor output power, C_{pr} is wind turbine rotor power coefficient. The C_{pw} and C_{pr} are the same for conventional wind turbine. For the CFJ wind turbine, the net power coefficient C_{pw} is defined as:

$$C_{pw} = C_{pr} - P_c \tag{8}$$

where P_c is the CFJ power coefficient defined in Eqn. 8.

4 Governing Equations

The governing equations are the Navier-Stokes equations in rotating frame with the effects of Coriolis force $(2\omega \times \mathbf{V})$ and centrifugal force $(\omega \times \omega \times \mathbf{r})$. The normalized Reynolds Averaged Navier-Stokes governing equations with Spalart–Allmaras one-equation turbulent model [22] in generalized coordinates are given by:

$$\frac{\partial \mathbf{Q}}{\partial t} + \frac{\partial \mathbf{E}}{\partial \xi} + \frac{\partial \mathbf{F}}{\partial \eta} + \frac{\partial \mathbf{G}}{\partial \zeta} = \frac{1}{Re}\left[\frac{\partial \mathbf{R}}{\partial \xi} + \frac{\partial \mathbf{S}}{\partial \eta} + \frac{\partial \mathbf{T}}{\partial \zeta}\right] + \mathbf{D} \tag{9}$$

where Re is the Reynolds number. The conservative variable vector $\mathbf{Q}$, invisid flux $\mathbf{E}$, viscous flux vector $\mathbf{R}$ and source term $\mathbf{D}$ are expressed as follows, and the rest can be expressed following the symmetric rule.

$$\mathbf{Q} = \frac{1}{J}\begin{bmatrix} \rho \\ \rho u \\ \rho v \\ \rho w \\ \rho e \\ \rho \hat{\nu} \end{bmatrix} \tag{10}$$

$$\mathbf{E} = \frac{1}{J} \begin{bmatrix} \rho U \\ \rho u U + p\xi_x \\ \rho v U + p\xi_y \\ \rho w U + p\xi_z \\ (\rho e + p)U \\ \rho \hat{\nu} U \end{bmatrix} \tag{11}$$

$$\mathbf{R} = \frac{1}{J} \begin{bmatrix} 0 \\ \tau_{xi}\xi_i \\ \tau_{yi}\xi_i \\ \tau_{zi}\xi_i \\ (u_j\tau_{ij} - q_i)\xi_i \\ \frac{\rho}{\sigma}(\nu + \hat{\nu})\frac{\partial \hat{\nu}}{\partial x_i}\xi_i \end{bmatrix} \tag{12}$$

$$\mathbf{D} = \frac{1}{J} \begin{bmatrix} 0 \\ 0 \\ \rho R_0{}^2 y + 2\rho R_0 w \\ \rho R_0{}^2 z - 2\rho R_0 v \\ 0 \\ S_\nu \end{bmatrix} \tag{13}$$

where R_0 is the Rossby number defined as $(\omega L_\infty)/U_\infty$. ω is the angular velocity of the rotor rotation, L_∞ is the reference length and U_∞ is the freestream velocity. The normalized equation of state as a constitutive equation relating density to pressure and temperature is expressed in the rotating frame as

$$\rho e = \frac{p}{\gamma - 1} + \frac{1}{2}\rho(u^2 + v^2 + w^2) - \frac{1}{2}\rho r^2 R_0{}^2 \tag{14}$$

The S_ν in Eq. (15) is the source term for the S-A model,

$$
\begin{aligned}
S_\nu = {} & \rho c_{b1}(1 - f_{t2})\tilde{S}\tilde{\nu} + \frac{1}{Re}\left[-\rho\left(c_{w1}f_w - \frac{c_{b1}}{\kappa^2}f_{t2}\right)\left(\frac{\tilde{\nu}}{d}\right)^2 \right. \\
& \left. + \frac{\rho}{\sigma}c_{b2}(\nabla\tilde{\nu})^2 - \frac{1}{\sigma}(\nu + \tilde{\nu})\nabla\tilde{\nu}\bullet\nabla\rho \right] + Re\left[\rho f_{t1}(\Delta q)^2\right]
\end{aligned} \tag{15}
$$

Other auxiliary relations and coefficients for the S-A turbulence model can be found in [22, 23].

5   Numerical Methods

The in-house high order accuracy CFD code Flow-Acoustics-Structure Interaction Package (FASIP) is used to conduct the numerical simulation. The 3D Reynolds Averaged Navier-Stokes (RANS) equations with one-equation Spalart-Allmaras [22] turbulence model described above are solved. A 3rd order MUSCL scheme for the inviscid flux [24, 25, 26] and a 2nd order central differencing for the viscous terms are employed to discretize the Navier-Stokes equations. The low diffusion Roe flux difference scheme is used to evaluate the inviscid fluxes. Implicit time marching method using Gauss-Seidel line relaxation is used to achieve a fast convergence rate [27]. Parallel computing is implemented to save wall clock simulation time [28]. The FASIP code is intensively validated for
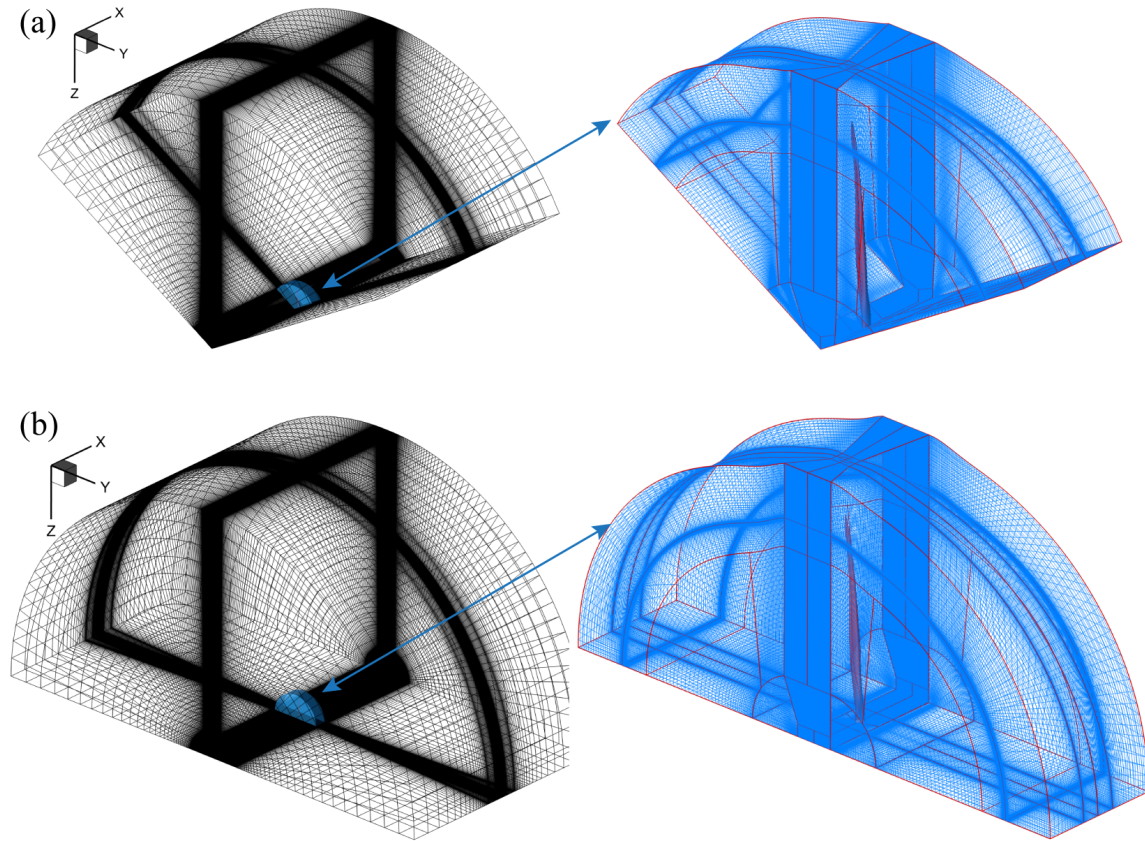
Figure 3: Mesh topology for (a) 3-bladed NREL RWT, (b) 2-bladed CFJ Wind Turbine

CFJ flow control simulations [3, 4, 5, 29, 30, 31, 32, 33, 34, 35], turbomachinery multistage flows[36, 37], and wind turbines [12, 13, 15].

Similar mesh topology used in [15] is adopted in this paper. The mesh size is $320 \times 280 \times 120$ in the circumferential, radial, and axial direction respectively. Only one blade is simulated with a $120°$ periodic boundary condition for the baseline 3-bladed turbine and a $180°$ periodic boundary condition for the CFJ 2-bladed turbine applied on the two circumferential boundaries of the computational domain originating from the hub. As shown in Fig. 3, the computational domain consists of a rotational inner domain (in blue) and a stationary outer domain (in black). The rotational domain is 3R in circumference and 2.5R in width. The stationary domain has a circumference of 6R and width of 8.5R. Frozen rotor boundary condition is applied on the interface between rotational and stationary domains with the blade located at zero azimuth. The mesh at the rotational frame and stationary frame are one-to-one connected to ensure flux conservation. The flow variables are converted between the rotational and stationary frames. The boundary conditions of total pressure, total temperature and flow angle are imposed at the upstream inlet boundary and the radial far field boundary of the stationary domain. A static pressure boundary condition is applied at the outlet boundary. The convergence criterion is that the L2-norm residual reduced by more than 4 orders of magnitude. The mesh size and number of points in each direction are similar to those used by other research groups in [38, 39]. The fist grid cell spacing is configured to ensure y^+ close to 1.

6   Results

This section will present the results and comparison analysis for the 3-bladed NREL RWT and the 2-bladed CFJ turbine. The optimized CFJ-NACA 64 series airfoils are used in the current CFJ Wind Turbine design. The corresponding chord, twisting, and bending distributions are kept the same as those of the 3-bladed 3.4 MW RWT rotor designed by National Renewable Energy Laboratory (NREL) [16]. The baseline blade and CFJ blade geometries are shown in Fig. 4. From the turbine root to 21.18% span, the CFJ turbine blade airfoil is the same as the baseline blade. The CFJ-NACA 64 series airfoils is used from 31.88% span to the turbine tip. Some wind turbine parameters are listed in Table 1. More details regarding the RWT blade geometry and designed performance can be found in [16].

Table 1: Wind turbine parameters used in the current study

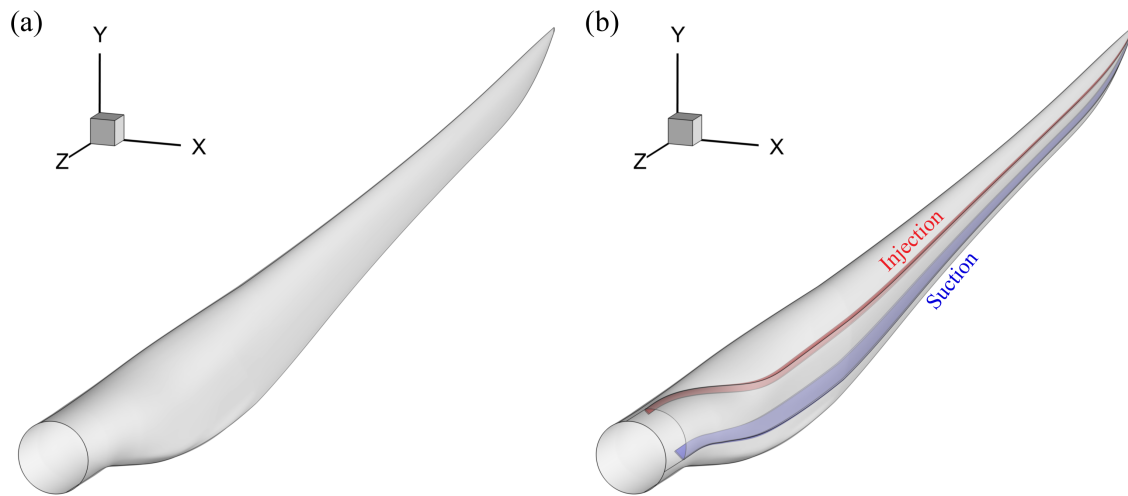| Rotor Orientation	Upwind
Number of blades	3 for RWT; 2 for CFJ
Rotor diameter	130 m
Hub height	110 m
Rotor Cone Angle	3°
Blade Root Flange Length	2 m

Figure 4: Geometry of the (a) NREL 3-bladed 3.4 MW reference wind turbine blade and (b) CFJ 2-bladed Wind Turbine blade

Three baseline RWT cases (B1-B3) and three CFJ cases (C1-C3) are compared and discussed in this section. The corresponding case parameters and simulation results are listed in Table 2 for comparison. Three freestream speed U_∞=4 m/s (cut in speed), 7 m/s, and 9.8 m/s (rated speed) are simulated in the current study. The wind turbine rotating speed ω at different U_∞ are varied to maintain the tip speed ratio (TSR) around 8.5 based on NREL's RWT design [16].

As listed in Table 2, the NREL baseline RWT cases (B1-B3) exhibits the wind turbine power coefficient C_{pw} about 0.45. For the CFJ Wind Turbine cases (C1-C3), the C_{pw} is increased significantly at all freestream speed. The CFJ Wind Turbine power is calculated by using CFJ fan efficiency of 85%. The maximum power gain is 25.9%

Table 2: Comparison of 3-bladed RWT and CFJ 2-bladed Wind Turbine power performance

Cases	$U_\infty(m/s)$	$\omega(RPM)$	$\theta(°)$	C_μ	P_C	C_{pw}	ΔP_{net}	$P_{net}(MW)$	$T_s(MN{\cdot}m)$	$T_b(MN{\cdot}m)$
B1	4	5.024	1.173	N/A	N/A	0.4446	N/A	0.229	0.146	1.232
C1	4	5.024	1.173	0.025	0.1006	0.5599	25.9%	0.289	0.325	5.199
B2	7	8.791	1.173	N/A	N/A	0.4454	N/A	1.230	0.446	3.750
C2	7	8.791	1.173	0.025	0.0931	0.5258	18.1%	1.452	0.930	9.269
B3	9.8	11.753	0.87	N/A	N/A	0.4495	N/A	3.406	0.923	7.165
C3	9.8	11.753	0.87	0.025	0.0845	0.5204	15.8%	3.944	1.862	15.027

with the U_∞=4 m/s. At the rated speed, the power gain is 15.8%. At lower speed, the CFJ power coefficient is much more improved than at high wind speed. This is very advantages to increase the annual power output or capacity factor as wind turbines will work at the speeds lower than the rated speed for most of the time.
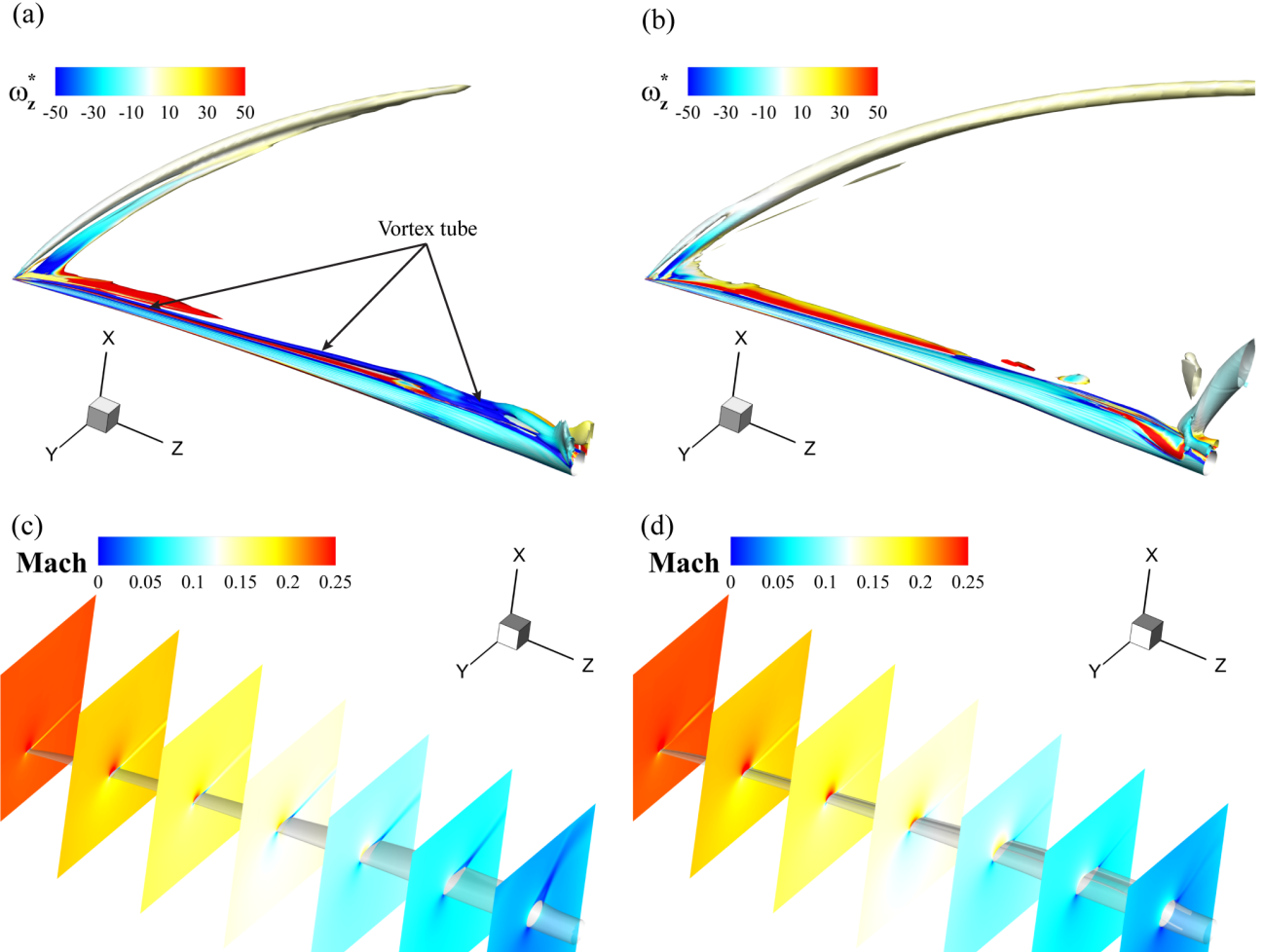

Figure 5: Iso-surface of λ_{max} colored by normalized z-direction vorticity ω_z of the case (a) B3 and (b) C3; Flow slices along the wind turbine blade span of case (c) B3 and (d) C3

The flow field around the turbine blade of the NREL baseline RWT and CFJ Wind Turbine is compared in Fig.

5. The cases with rated speed (B3 and C3) are chosen for the demonstration. Fig. 5 shows the vortical structures (iso-surface of λ_{max}, colored by normalized z-direction vorticity ω_z^*) and flow slices (Mach contours) along the turbine blade for the two cases. As shown in Fig. 5 (a), a long vortex tube can be observed above the trailing edge of the blade, connecting the blade root and tip. The vortex tube is formed by separated flow from the suction surface of the RWT blade for the case B3. Such vortex tube is not observed from the CFJ case C3, which suggests a much better flow attachment of the case C3. In addition, a slender blade tip vortex can be observed for both cases. The tip vortex of case C3 is stronger comparing to that of the case B3 since the blade loading of the CFJ Wind Turbine is much higher due to the reduced number of blades used and better flow attachment.
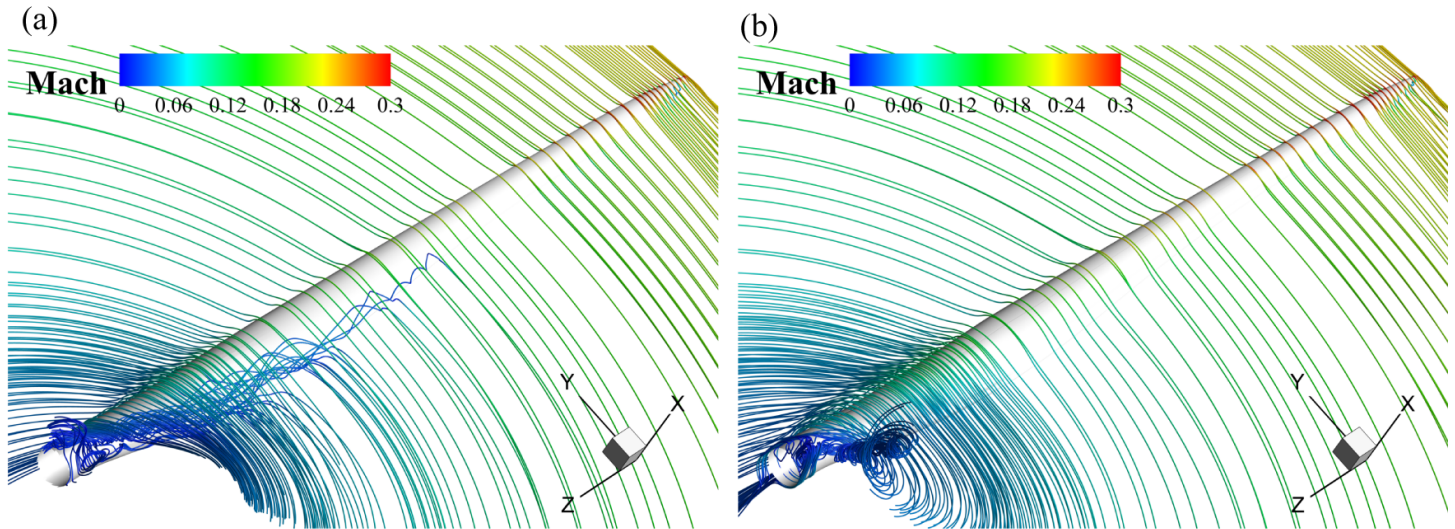

Figure 6: 3D streamlines around turbine blades for the case (a) B3 and (b) C3

As shown in Fig. 5 (c) and (d), flow separation can be observed at lower span of the blade for case B3. The CFJ blade of case C3 has the flow very well attached even at the lower span. Moreover, larger high speed zone can be identified near the leading edge of the blade for the case C3, which indicates a much higher blade loading.

Fig. 6 compares the 3D streamlines colored by Mach number around the turbine blade of the case B3 and C3. For the case B3, a root vortex can be observed downstream of the cylinder shape turbine root. In addition, large flow separation can be identified at lower blade span (r/R<50%) above the trailing edge of the blade. For the case C3, similar vortex can also be found downstream of the turbine root, where the CFJ flow control is not applied. For other part of the CFJ Wind Turbine, very well flow attachment is observed due to the CFJ active flow control even though the 2-bladed CFJ blade loading is much higher than the 3-bladed RWT.

Flow slices along the blade span are presented in Fig. 7 for the case B3 and C3. For the case B3, at lower blade span (Fig. 7 a and d), large flow separation can be observed near the blade trailing edge. At higher blade span (Fig. 7 g and j), flow separation still exist but with lower intensity. The NREL baseline RWT has low AoA at higher span to prevent large flow separation. For the case C3, no flow separation can be observed at all blade spans (Fig. 7 b, e, h, k). In addition, much larger high speed acceleration zone is observed at the blade suction surface for all blade spans due to the higher loading.
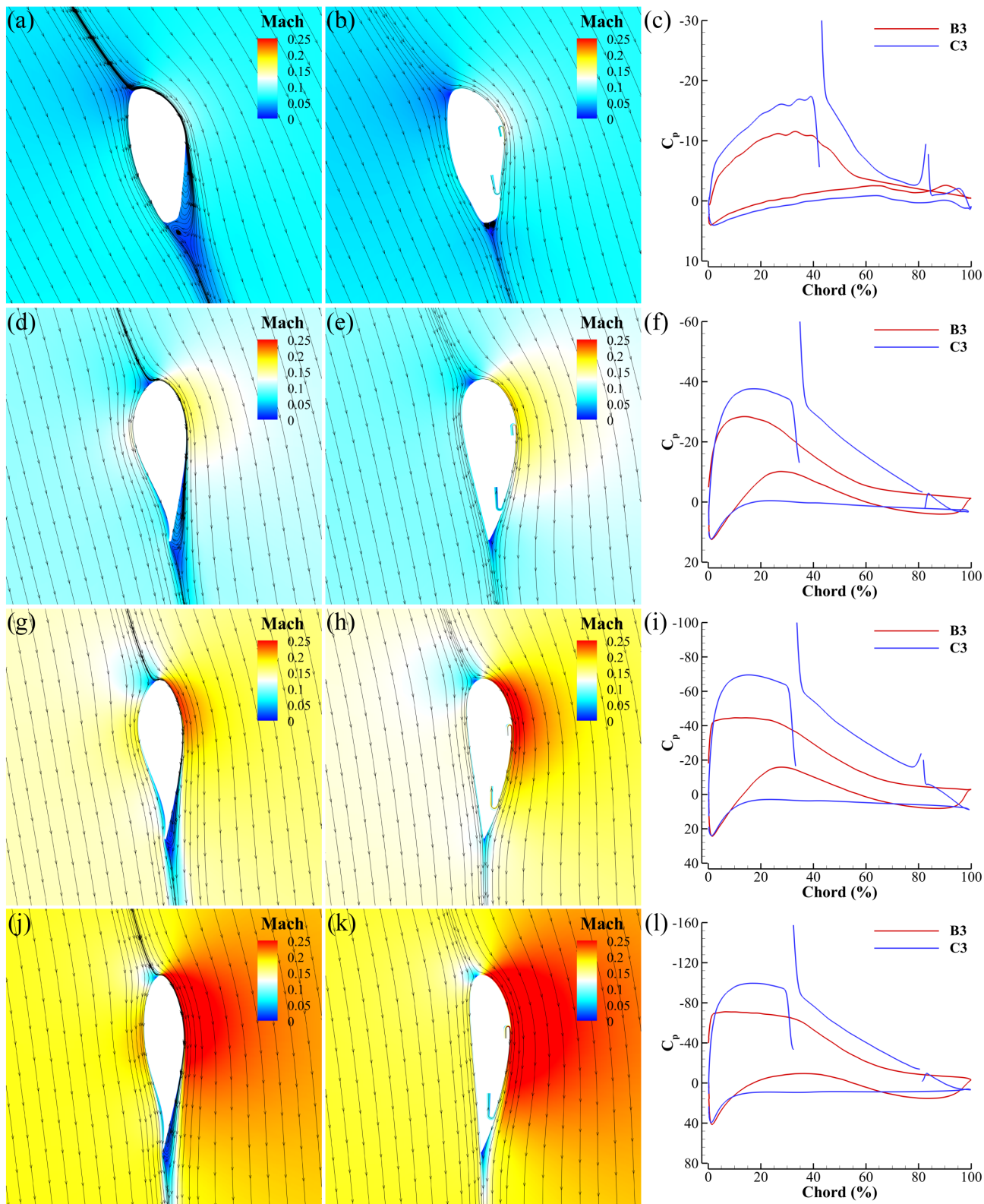
Figure 7: Flow slices at r/R=20%, 40%, 60%, and 80% for the case B3 (a, d, g, j) and case C3 (b, e, h, k); C_p distribution of the case B3 and C3 at (c) r/R=20%, (f) r/R=40%, (i) r/R=60%, (l) r/R=80%.

The surface pressure coefficient C_p distribution of the two turbines are shown in Fig. 7 (c), (f), (i), and (l) for the blade span r/R=20%, 40%, 60%, and 80%, respectively. Fig. 7 indicates that CFJ Wind Turbine (case C3) has a more desirable C_p distribution comparing with the NREL baseline RWT (case B3). The CFJ case C3 has the suction peak located at around 20% chord and linearly increase towards trailing edge. The C_p on the pressure surface are almost constant. The CFJ airfoil exhibits a chordwise front loading distribution and the loading linearly decreases to the trailing edge. For the baseline case B3, the C_p also shows a front loading, but the loading remains fairly constant after 30% chord to the trailing edge and causes flow separation near the trailing edge.
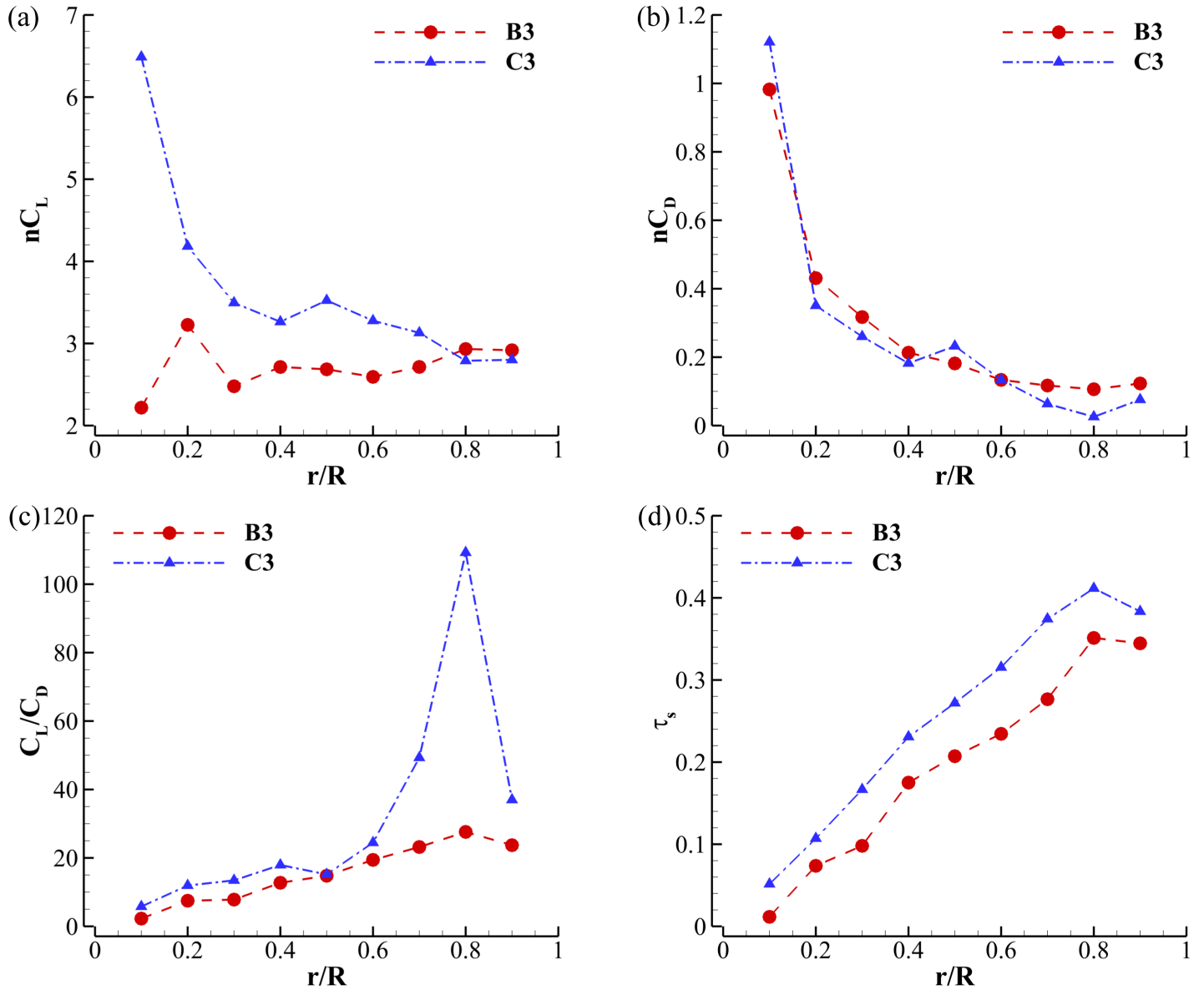

Figure 8: (a) C_L, (b) C_D, (c) C_L/C_D, (d) τ_s distribution along the blade span for the case B3 and C3. All blades of the wind turbine are included in the integration (n stands for the number of blades of a turbine).

Fig. 8 shows the distribution of C_L, C_D, C_L/C_D, and τ_s along the blade span normalized by the relative speed

at the local radius for the two cases. We can see that case C3 exhibits a much higher C_L, much lower C_L/C_D at almost all spans, which is due to the CFJ flow control prevent flow separation and greatly improve the blade loading and efficiency.

The C_L increase is particularly more for the inner 20% span since the airfoil configuration is mostly cylinder, which does not generate much lift and power for the baseline blade. But CFJ cylinder can generate very high lift with no flow separation [40]. Eqn. 2 shows that higher C_L and lower C_L/C_D results in higher power output, which is consistent with the spinning torque coefficient τ_s distribution shown in Fig. 8 (d). The τ_s of the CFJ wind turbine is consistently higher than that of the baseline RWT along the entire span. It is worth noting that the CFJ turbine shows large torque improvement even near the blade root. The τ_s at r/R=10% for the CFJ wind turbine is 3.45 times greater than that of the baseline RWT.
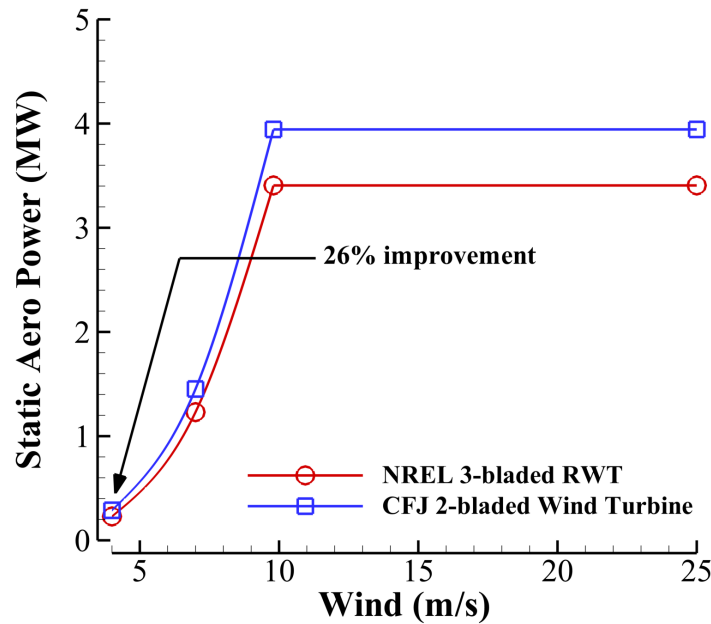

Figure 9: Static aerodynamic power of the NREL baseline wind turbine and CFJ Wind Turbine

Fig. 9 shows the simulated static aerodynamic power of the NREL 3-bladed baseline RWT and CFJ 2-bladed Wind Turbine at different wind speed. Fig. 9 is the reflection of the results in Table 2. We can see that the rated power of the CFJ 2-bladed Wind Turbine reaches 4 MW while the NREL baseline 3-bladed RWT rated power is 3.4 MW, 15.8% power increase as indicated in Table 2. At low speed, the power increase is even more up to 26%. Such a performance improvement will make the capacity factor increase more than 20%. This study is just an initial effort to demonstrate the advantage of the CFJ blade with no design optimization. It is believed that there is more potential to further enhance the efficiency improvement.

7   Conclusions

A 2-bladed CFJ utility wind turbine is numerically designed and simulated based on the NREL 3-bladed 3.4 MW reference wind turbine with the distribution of chord, twist, and bending kept the same. The CFJ 2-bladed wind turbine adopts the CFJ-NACA 64 series airfoils at most of the blade span from 31.88% to the tip. The CFJ injection and suction slots are implemented along the blade span to achieve CFJ active flow control. The study

shows that the 2-bladed CFJ turbine significantly increases power output compared with the 3-bladed baseline turbine at all wind speeds by 15.8% at the wind speed of 9.8 m/s and by 25.9% at 4 m/s respectively. The efficiency enhancement is substantially more at the low wind speed than at high wind speed. This would be very beneficial to increase the annual power output or capacity factor as wind turbines work at the speeds lower than the rated speed for most of the time. The results show that the flow field around the blade surface presents a significant enhanced suction peak near the blade leading edge, which results in a very high tangential force and thus increased wind turbine net power coefficient. Consistent with the previous study for the small NREL Phase VI research wind turbine, this paper demonstrates that CFJ 2-bladed wind turbine is an effective technology to extract high power from the wind at all speeds. This study is just an initial effort to demonstrate the advantage of the CFJ blade with no design optimization. It is believed that there is more potential to further enhance the efficiency improvement.

References

[1] N. Johnson, P. Bortolotti, G. Dykes, K. Barter, P. Moriarty, S. Carron, F. Wendt, P. Veers, J. Paquette, C. Kelly, and B. Ennis, "Investigation of innovative rotor concepts for the big adaptive rotor project." Technical Report NREL/TP-5000-73605, September 2019.

[2] G.-C. Zha, B. F Carroll, C. D. Paxton, C. A. Conley, and A. Wells, "High-performance airfoil using coflow jet flow control," *AIAA journal*, vol. 45, no. 8, pp. 2087–2090, 2007.

[3] A. Lefebvre, B. Dano, W. Bartow, M. Fronzo, and G. Zha, "Performance and energy expenditure of coflow jet airfoil with variation of mach number," *Journal of Aircraft*, vol. 53, no. 6, pp. 1757–1767, 2016.

[4] G. Zha, W. Gao, and C.D. Paxton, "Jet Effects on Co-Flow Jet Airfoil Performance," *AIAA Journal*, vol. 45, pp. 1222–1231, 2007.

[5] G.-C. Zha, C. Paxton, A. Conley, A. Wells, nd B. Carroll, "Effect of Injection Slot Size on High Performance Co-Flow Jet Airfoil," *AIAA Journal of Aircraft*, vol. 43, pp. 987–995, 2006.

[6] Yang, Yunchao and Zha, Gecheng, "Super-Lift Coefficient of Active Flow Control Airfoil: What is the Limit?," *AIAA SCITECH2017, 55th AIAA Aerospace Science Meeting, Grapevine, Texas*, AIAA 2017-1693.

[7] J. Zhang, K. Xu, Y. Yang, Y. Ren, P. Patel, and G. Zha, "Aircraft control surfaces using co-flow jet active flow control airfoil." AIAA Paper 2018-3067, 2018 Applied Aerodynamics Conference, Atlanta, Georgia, June 25-29, 2018.

[8] K. Xu, J. Zhang, and G. Zha, "Drag minimization of co-flow jet control surfaces at cruise conditions." AIAA 2019-1848, AIAA Scitech 2019 Forum, San Diego, California, 7-11 January 2019.

[9] Xu, Kewei and Zha, Gecheng, "System energy benefit using co-flow jet active separation control for a serpentine duct," *Elsevier Journal of Aerospace Science and Technology*, vol. 128, p. DOI: 10.1016/j.ast.2022.107746, 2022.

[10] Xu, Kewei and Ren, Yan and Zha, Gecheng, "Numerical Analysis of Energy Expenditure for Co-Flow Wall Jet Separation Control ," *AIAA Journal*, vol. 60, no. 5, p. doi.org/10.2514/1.J061015, 2022.

[11] A. Lefebvre and G. Zha, "Numerical simulation of pitching airfoil performance enhancement using co-flow jet flow control," vol. 2517, 2013.

[12] K. Xu and G. Zha, "Investigation of coflow jet active flow control for wind turbine airfoil." AIAA Paper will be virtually presented in 2020 AIAA AVIATION Forum and Exposition, AIAA 2020-2942, 15-19 June, 2020.

[13] K.-W. Xu and G.-C. Zha, "High efficiency wind turbine using co-flow jet active flow control." ASME Paper GT2021-59664, Proceedings of ASME Turbo Expo 2021 Turbomachinery Technical Conference and Exposition, Virtual, Online, June 07-11, 2021.

[14] D. Simms, S. Schreck, M. Hand, and L. J. Fingersh, "NREL unsteady aerodynamics experiment in the NASA-Ames wind tunnel: a comparison of predictions to measurements," tech. rep., National Renewable Energy Lab., Golden, CO (US), 2001.

[15] Y. Ren, K. Xu, and G. Zha, "Wind turbine efficiency enhancement by coflow jet airfoil," in *AIAA 2022-1787, AIAA SCITECH 2022 Forum*, p. 1787, 2022.

[16] P. Bortolotti, H. C. Tarres, K. L. Dykes, K. Merz, L. Sethuraman, D. Verelst, and F. Zahle, "IEA Wind TCP Task 37: Systems engineering in wind energy-wp2. 1 reference wind turbines," tech. rep., National Renewable Energy Lab.(NREL), Golden, CO (United States), 2019.

[17] Burton, T. and Jenkins, N. and Sharpe, D. and Bossanyi, E., "Wind Energy Handbook, 2nd Edition." ISBN: 978-0-470-69975-1, Wiley, June 2011.

[18] J. Manwell, J. McGowan, and A. Rogers, *Wind Energy Explained Theory, Design and Application.* ISBNs: 0-471-49972-2: John Wiley & Sons Ltd, 2002.

[19] Thumthae, C. and Chitsomboon, T., " Optimal angle of attack for untwisted blade wind turbine," *Renewable Energy*, vol. 34, pp. 1279–1284, 2009.

[20] S. A. Huyer, D. Simms, and M. C. Robinson, "Unsteady aerodynamics associated with a horizontal-axis wind turbine," *AIAA journal*, vol. 34, no. 7, pp. 1410–1419, 1996.

[21] Lefebvre, A. and Dano, B. and Bartow, W. and Di Franzo, M. and Zha, G.-C., "Performance and Energy Expenditure of Coflow Jet Airfoil with Variation of Mach Number." AIAA Paper 2013-0490, AIAA Journal of Aircraft, DOI: 10.2514/1.C033113, 2016.

[22] P. Spalart and S. Allmaras, "A One-equation Turbulence Model for Aerodynamic Flows." AIAA-92-0439, 30th Aerospace Sciences Meeting and Exhibit, Reno,NV,U.S.A., 06 January 1992 - 09 January 1992.

[23] B.-Y. Wang, B. Haddoukessouni, J. Levy, and G.-C. Zha, "Numerical Investigations of Injection Slot Size Effect on the Performance of Co-Flow Jet Airfoil." AIAA Paper 2007-4427, 2007.

[24] Y.-Q. Shen, G.-C. Zha, and B.-Y. Wang, "Improvement of Stability and Accuracy of Implicit WENO Scheme ," *AIAA Journal*, vol. 47, pp. 331–344, 2009.

[25] Shen, Y.-Q. and Zha, G.-C. and Chen, X.-Y., " High Order Conservative Differencing for Viscous Terms and the Application to Vortex-Induced Vibration Flows," *Journal of Computational Physics*, vol. 228(2), pp. 8283–8300, 2009.

[26] Shen, Y.-Q. and Zha, G.-C. , " Improvement of the WENO Scheme Smoothness Estimator," *International Journal for Numerical Methods in Fluids*, vol. DOI:10.1002/fld.2186, 2009.

[27] G.-C. Zha and E. Bilgen, "Numerical study of three-dimensional flows using unfactored upwind-relaxation sweeping algorithm," *Journal of Computational Physics*, vol. 125, no. 2, pp. 425–433, 1996.

[28] B. Wang, Z. Hu, and G.-C. Zha, "General subdomain boundary mapping procedure for structured grid implicit cfd parallel computation," *Journal of Aerospace Computing, Information, and Communication*, vol. 5, no. 11, pp. 425–447, 2008.

[29] B. Wang, B. Haddoukessouni, J. Levy, and G.-C. Zha, "Numerical investigations of injection-slot-size effect on the performance of coflow jet airfoils," *Journal of Aircraft*, vol. 45, no. 6, pp. 2084–2091, 2008.

[30] Lefebvre, A. and Zha, G.-C. , "Design of High Wing Loading Compact Electric Airplane Utilizing Co-Flow Jet Flow Control." AIAA Paper 2015-0772, AIAA SciTech2015: 53nd Aerospace Sciences Meeting, Kissimmee, FL, 5-9 Jan 2015.

[31] Liu, Z.-X. and Zha, G.-C., "Transonic Airfoil Performance Enhancement Using Co-Flow Jet Active Flow Control." AIAA Paper 2016-3066, AIAA Aviation, Washington, D.C., June 13-17 2016.

[32] Lefebvre, A. and Zha, G.-C., "Trade Study of 3D Co-Flow Jet Wing for Cruise Performance." AIAA Paper 2016-0570, AIAA SCITECH2016, AIAA Aerospace Science Meeting, San Diego, CA, 4-8 January 2016.

[33] B. Wang and G.-C. Zha, "Detached-eddy simulation of a coflow jet airfoil at high angle of attack," *Journal of aircraft*, vol. 48, no. 5, pp. 1495–1502, 2011.

[34] Y. Yang and G. Zha, "Super-lift coefficient of active flow control airfoil: What is the limit?." AIAA Paper 2017-1693, AIAA SCITECH2017, 55th AIAA Aerospace Science Meeting, Grapevine, January 9-13 2017.

[35] Im, H.-S and Zha, G.-C. and Dano, B. P. E., "Large Eddy Simulation of Coflow Jet Airfoil at High Angle of Attack," *Journal of Fluid Engineering, vol. 136(2), p. 021101*, 2014.

[36] D. Espinal, H.-S. Im, and G.-C. Zha, "Full-annulus simulation of nonsynchronous blade vibration excitation of an axial compressor," *Journal of Turbomachinery*, vol. 140, no. 3, 2018.

[37] H. Iim, X.-Y. Chen, and G. Zha, "Detached-eddy simulation of rotating stall inception for a full-annulus transonic rotor," *Journal of Propulsion and Power*, vol. 28, no. 4, pp. 782–798, 2012.

[38] S. A. Tran, D. A. Corson, and O. Sahni, "Synthetic jet based active flow control of dynamic stall phenomenon on wind turbines under yaw misalignment," in *32nd ASME Wind Energy Symposium*, p. 0871, 2014.

[39] A. L. Pape and J. Lecanu, "3d navier–stokes computations of a stall-regulated wind turbine," *Wind Energy: An International Journal for Progress and Applications in Wind Power Conversion Technology*, vol. 7, no. 4, pp. 309–324, 2004.

[40] Y. Yang and G. Zha, "Super lift coefficient of cylinder using co-flow jet active flow control," in *Proceedings of the 2018 AIAA Aerospace Sciences Meeting, Kissimmee, FL, USA. AIAA Paper 2018-0329*, pp. 8–12, 2018.